LINEAR MULTIMODAL MODEL FOR A PRESSURIZED GAS BLADDER STYLE HYDRAULIC NOISE SUPPRESSOR

Kenneth A. Marek, Elliott R. Gruber and Kenneth A. Cunefare

G. W. Woodruff School of Mechanical Engineering, Georgia Institute of Technology, 771 Ferst Dr., Atlanta, GA 30332, USA
ken.marek@gatech.edu, e_gruber@gatech.edu, ken.cunefare@me.gatech.edu

Abstract

Pressurized bladder style in-line hydraulic noise suppressors are commonly used in industry for broadband pressure ripple reduction, but predictive models for these suppressors are not available in the literature. To address this shortcoming, a linear acoustic model is developed for a commercially available suppressor, in which the acoustic field is analyzed through expansion into multiple radial modes. Bladder mass, perforate layer impedance, and inlet/outlet extensions are included in the model, and transmission loss predictions are validated against experimental data. The presented theoretical model has been shown to correspond well to experimental data at frequencies below about 1300 to 2300 Hz, depending on system and precharge pressures. In addition, simulations show that small variations in bladder precharge temperature or rubber bladder mass do not significantly affect transmission loss. While inclusion of the perforate layer significantly affects modeling results, it is observed that better perforate layer models or experimental data are needed for accurate system modeling.

Keywords: hydraulic, silencer, suppressor, model

1 Introduction

Pressurized bladder devices have been used in hydraulic equipment for many years for energy storage and fluid noise mitigation. Such devices usually employ nitrogen as the gas of choice, filling a bladder-backed cavity to a specified precharge pressure before the hydraulic system is brought to working pressure. For example, side branch accumulators contain a gas pressurized bladder, and are commonly used to store energy, compensate for fluid volume changes, or reduce shock loads. These devices act as low-pass filters of acoustic noise as well. A few studies examine noise mitigation from accumulators, including water hammer suppression (Rabie, 2007) and an active accumulator to attenuate specific frequencies of excitation (Yokota et al., 1996). While some device sizing and precharge recommendations are available from general handbooks and literature from the manufacturer or distributor, and the use of accumulators is quite common in industry to relieve fluid noise, no published noise control models have been found. In contrast, in-line bladder devices are developed for the explicit purpose of noise control (Dexter, 1985; Jenski and Shiery, 1998; Shiery, 1998), usually broad-band. At least one type (Arendt, 1988) is commercially available, but the modeling situation is much the same. Limited test data (Wilkes, 1995) have been presented for the commercial device, but frequency domain noise control characteristics have been difficult to find, and no modeling data have been uncovered in this respect.

Due to the wide range of applications and operating conditions found in hydraulic equipment, both linear and nonlinear behavior could potentially be expected from a silencing device. For this study, only linear response will be considered, corresponding to lower amplitude noise excitation. In this case, a number of models are available which characterize silencers of similar geometry for air ducting applications. Some finite element and boundary element models of these silencers have been developed (Bilawchuk and Fyfe, 2003; Denia et al., 2007; Lee et al., 2006; Selamet and Ji, 1999), often in conjunction with modal expansion solutions, which are also prevalent. These latter models provide the basis for the present model of a bladder style silencer. Among the less complex models, Peat (1991) finds a transfer matrix for a liner element, and other researchers produce transmission loss predictions for a simple lined expansion chamber configuration (Kirby, 2001; Xu et al., 2003). More

This manuscript was received on 19 October 2012 and was accepted after revision for publication on 16 May 2013

complex geometry can be considered by explicitly examining the effects of a perforated annulus (Selamet et al., 2004). The perforated annulus is modeled as an impedance layer in this type of analysis; and although theoretical models have been developed, such as in chapter 9 of Bies and Hansen (2009), the published silencer models have instead relied on experimental impedance studies (Sullivan and Crocker, 1978), some of which include the effects of grazing flow (Dickey et al., 2001) or resistive backing materials (Kirby and Cummings, 1998; Lee et al., 2006). Several studies have examined silencers with both perforate layers and inlet/outlet extensions as well (Denia et al., 2007; Selamet and Ji, 1999; Selamet et al., 2005). Additional studies have included mean flow in the liner (Cummings and Chang, 1988; Kirby and Denia, 2007; Nennig et al., 2010), which is only applicable to fibrous or porous liners. Panigrahi and Munjal (2005) give a brief overview of some of the varying levels of model complexity.

Many aspects of these models are applicable to a bladder style hydraulic suppressor, but important differences exist. First, the hydraulic suppressor is under significant pressure, and the system pressure affects the response of the compressed gas. Second, while the air silencers have a porous or fibrous liner which primarily adds damping to the system, the compressed gas behind the suppressor bladder is expected to add significant compliance but not necessarily damping. Both types of devices may have a perforated annulus which adds some acoustic or structural value, but additionally the hydraulic suppressor contains the physical bladder layer which separates the compressed gas from the hydraulic fluid. The rubber bladder and perforate layer may add damping to the system. Finally, although many air silencer models include the mean flow speed as a Mach flow number, the flow speed in a hydraulic suppressor is generally much lower than the speed of sound in hydraulic fluid, and can be ignored. The model developed in this study is similar to Selamet et al. (2005). The notable differences are a different mode matching scheme as discussed in the derivation, the addition of a mass model to estimate the rubber bladder influence, and the examination of a theoretical perforate impedance model since experimental impedance data are not available. The effects of temperature, bladder density, and perforate impedance are studied, and results are experimentally validated.

2 Model Geometry

The various components of the suppressor under consideration are shown in Fig. 1. There is an inner cylindrical flow path; a coarse perforation layer (hydraulic fluid travels through this layer to reach an outer chamber); a spacer in the form of a compression spring; and a thin, finely perforated layer. Outside the perforated section, a rubber bladder separates the hydraulic fluid from the pressurized nitrogen gas in the outermost section of the chamber. The thin perforate layer and rubber bladder are shown removed from the main assembly in part (a) of the Fig. 1; the spring separator is omitted in part (b). Dimension labels are shown in Fig. 2. The inlet and outlet pipe radius is r_0. The length of the suppressor is L plus inlet and outlet extension lengths L_1 and L_2. When the bladder is precharged to pressure P_c but the hydraulic system is unpressurized, the gas expands so that the bladder reaches the thin perforate layer at r_1; when the hydraulic system is pressurized to P_s, the gas compresses further and is constrained between the rigid outer shell at r_2 and the rubber bladder at r_3.

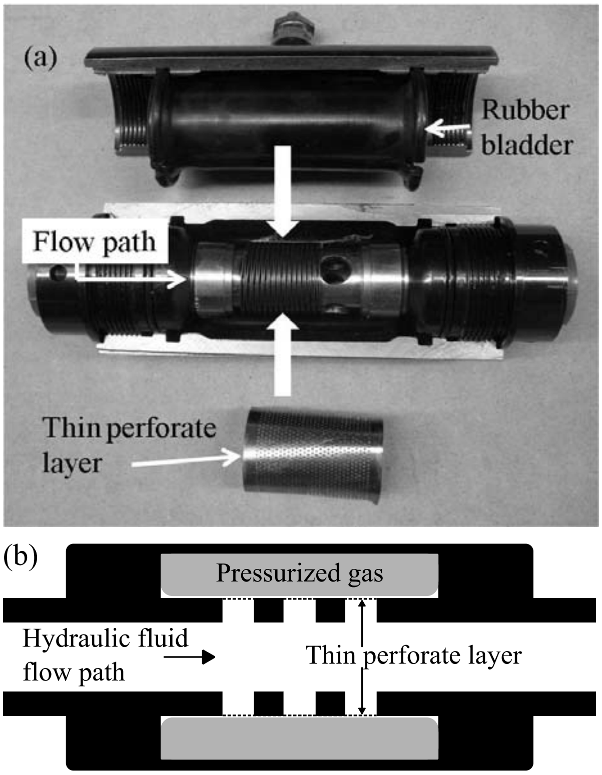

Fig. 1: *Suppressor features. (a) Photograph of device cross section with thin perforate layer and rubber bladder removed from main body; (b) Modeling diagram showing thin perforate layer and bladder in place*

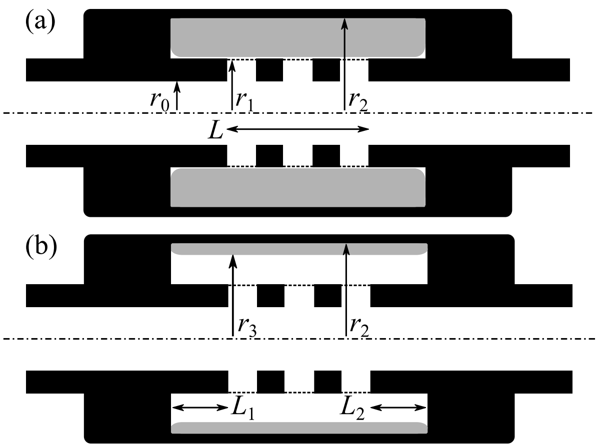

Fig. 2: *Suppressor geometry with dimensions for (a) unpressurized system, (b) pressurized system. When the system is not pressurized, the bladder is pushed against the thin perforate layer at r_1; when system pressure is applied, the bladder moves to equilibrium at r_3*

Bladder radius r_3 is determined by the suppressor geometry, as well as charge and system pressures P_c

and P_s. When the bladder is precharged with nitrogen, the gas volume is known to be

$$V_0 = \pi L_T \left(r_2^2 - r_1^2 \right), \tag{1}$$

where

$$L_T = L + L_1 + L_2 . \tag{2}$$

The mass of the nitrogen is found using the ideal gas law:

$$m = \frac{M_N P_c V_0}{R T_0}, \tag{3}$$

for molar mass M_N, temperature T_0 in Kelvins, and universal gas constant R. At full system pressure P_s and working temperature T, the nitrogen mass remains constant, and the bladder radius is found by solving

$$V = \frac{mRT}{M_N P_s} = \pi L_T \left(r_2^2 - r_3^2 \right), \tag{4}$$

from which r_3, the bladder radius, may be found. For this analysis to be valid, P_s must be greater than P_c.

The density ρ_f and sound speed c_f in the hydraulic fluid are assumed to be known and not to change with varying pressure or temperature. Additionally, the bladder at r_3 is treated as a limp mass sheet with sheet density σ_s calculated from the bladder mass, length, and diameter at P_s. For bladder mass m_b distributed evenly over length L_T,

$$\sigma_s = \frac{m_b}{2\pi r_3 L_T} . \tag{5}$$

3 Acoustic Propagation Model

For modeling purposes, the suppressor is divided into three axial regions, as shown in Fig. 3. Region 1 includes the upstream (1U) and downstream (1D) pipes; region 2 represents the main body of the suppressor section, including the main hydraulic fluid flow path as well as the thin perforate layer, rubber bladder, and compressed nitrogen gas; and region 3 contains the upstream (3U) and downstream (3D) extension sections, including hydraulic fluid, rubber bladder, and compressed nitrogen layers. In general, the regions are referred to by number, with the U or D added only if the quantity differs between the upstream and downstream portions. The axial references $x = 0$ and $x = L$ are also shown, with the positive x direction facing right. As illustrated in Fig. 4, each region R has forward and reverse travelling modes with unique modal amplitudes $A_{R,n}$ and $B_{R,n}$ for N modes, where n = 0 to N - 1. For waves in regions 1U, 2, and 3U, modal amplitudes represent their values at $x = 0$; for regions 1D and 3D, they are found at $x = L$.

The elasticity of the hydraulic fluid and nitrogen gas (the "liner") are represented by Lamé parameters λ_f and λ_L, respectively. Shear moduli μ_f and μ_L are both zero for these materials, thus making λ_f and λ_L equivalent to the bulk moduli of the propagation media. This also means that only longitudinal waves will propagate in the suppressor. Sound speeds are defined as:

$$c_f = \sqrt{\frac{\lambda_f}{\rho_f}}, \tag{6}$$

$$c_L = \sqrt{\frac{\lambda_L}{\rho_L}} . \tag{7}$$

And for angular frequency ω, wavenumbers k are defined as:

$$k_f = \frac{\omega}{c_f}, \quad k_L = \frac{\omega}{c_L} . \tag{8}$$

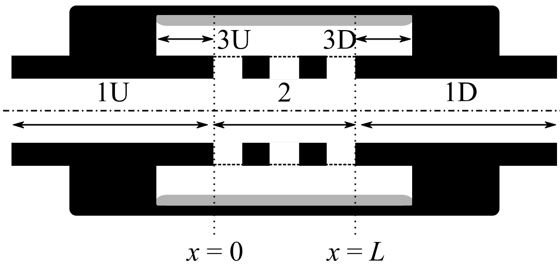

Fig. 3: *Model geometry with region labels*

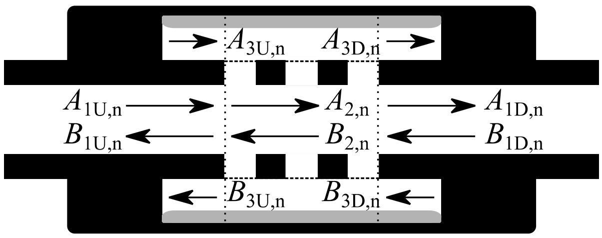

Fig. 4: *Model geometry with wave pressure amplitude labels*

For each propagation mode n and region R, the wavenumbers may be decomposed into axial and radial components, represented by subscripts x and r. These relate to the wavenumbers by

$$k_f^2 = k_{Rx,n}^2 + k_{Rrf,n}^2 \tag{9}$$

$$\text{and } k_L^2 = k_{Rx,n}^2 + k_{RrL,n}^2 . \tag{10}$$

Notably, in the suppressor, the axial wavenumber is the same in the hydraulic fluid as in the nitrogen, while the radial wavenumber differs in general, resulting in an additional subscript f or L to denote the medium. The acoustic displacements $u_{Rr,n}$ and $u_{Rx,n}$ in the respective radial and axial directions, are for the forward travelling modes given in Eq. 11 to 20. J_i and Y_i are i^{th} order Bessel functions of the first and second kind, relative complex amplitudes of coefficients $y_{1,n}$ to $y_{5,n}$ and $y_{6,n}$ to $y_{9,n}$ are unique for each mode n in regions 2 and 3, and $x = x' - L$. Similarly, acoustic pressures $p_{R,n}$ are given in Eq. 21 to 25.

$$u_{1Ur,n} = -k_{1rf,n} J_1 \left(k_{1rf,n} r \right) A_{1U,n}\, e^{-ik_{1x,n}x}\, e^{i\omega t}, \tag{11}$$

$$u_{1Dr,n} = -k_{1rf,n} J_1 \left(k_{1rf,n} r \right) A_{1D,n}\, e^{-ik_{1x,n}x'}\, e^{i\omega t}, \tag{12}$$

$$u_{2\mathrm{r,n}} = \begin{cases} -k_{2\mathrm{rf,n}} y_{1,\mathrm{n}} \mathrm{J}_1\left(k_{2\mathrm{rf,n}} r\right) A_{2,\mathrm{n}}\, \mathrm{e}^{-\mathrm{i}k_{2\mathrm{x,n}}x}\, \mathrm{e}^{\mathrm{i}\omega t},\ r < r_1 \\ -k_{2\mathrm{rf,n}} \left(y_{2,\mathrm{n}} \mathrm{J}_1\left(k_{2\mathrm{rf,n}} r\right) + y_{3,\mathrm{n}} \mathrm{Y}_1\left(k_{2\mathrm{rf,n}} r\right)\right) A_{2,\mathrm{n}}\, \mathrm{e}^{-\mathrm{i}k_{2\mathrm{x,n}}x}\, \mathrm{e}^{\mathrm{i}\omega t},\ r_1 \le r < r_3 \\ -k_{2\mathrm{rL,n}} \left(y_{4,\mathrm{n}} \mathrm{J}_1\left(k_{2\mathrm{rL,n}} r\right) + y_{5,\mathrm{n}} \mathrm{Y}_1\left(k_{2\mathrm{rL,n}} r\right)\right) A_{2,\mathrm{n}}\, \mathrm{e}^{-\mathrm{i}k_{2\mathrm{x,n}}x}\, \mathrm{e}^{\mathrm{i}\omega t},\ r \ge r_3 \end{cases}, \tag{13}$$

$$u_{3\mathrm{Ur,n}} = \begin{cases} -k_{3\mathrm{rf,n}} \left(y_{6,\mathrm{n}} \mathrm{J}_1\left(k_{3\mathrm{rf,n}} r\right) + y_{7,\mathrm{n}} \mathrm{Y}_1\left(k_{3\mathrm{rf,n}} r\right)\right) A_{3\mathrm{U,n}}\, \mathrm{e}^{-\mathrm{i}k_{3\mathrm{x,n}}x}\, \mathrm{e}^{\mathrm{i}\omega t},\ r < r_3 \\ -k_{3\mathrm{rL,n}} \left(y_{8,\mathrm{n}} \mathrm{J}_1\left(k_{3\mathrm{rL,n}} r\right) + y_{9,\mathrm{n}} \mathrm{Y}_1\left(k_{3\mathrm{rL,n}} r\right)\right) A_{3\mathrm{U,n}}\, \mathrm{e}^{-\mathrm{i}k_{3\mathrm{x,n}}x}\, \mathrm{e}^{\mathrm{i}\omega t},\ r \ge r_3 \end{cases}, \tag{14}$$

$$u_{3\mathrm{Dr,n}} = \begin{cases} -k_{3\mathrm{rf,n}} \left(y_{6,\mathrm{n}} \mathrm{J}_1\left(k_{3\mathrm{rf,n}} r\right) + y_{7,\mathrm{n}} \mathrm{Y}_1\left(k_{3\mathrm{rf,n}} r\right)\right) A_{3\mathrm{D,n}}\, \mathrm{e}^{-\mathrm{i}k_{3\mathrm{x,n}}x'}\, \mathrm{e}^{\mathrm{i}\omega t},\ r < r_3 \\ -k_{3\mathrm{rL,n}} \left(y_{8,\mathrm{n}} \mathrm{J}_1\left(k_{3\mathrm{rL,n}} r\right) + y_{9,\mathrm{n}} \mathrm{Y}_1\left(k_{3\mathrm{rL,n}} r\right)\right) A_{3\mathrm{D,n}}\, \mathrm{e}^{-\mathrm{i}k_{3\mathrm{x,n}}x'}\, \mathrm{e}^{\mathrm{i}\omega t},\ r \ge r_3 \end{cases}, \tag{15}$$

$$u_{1\mathrm{Ux,n}} = -\mathrm{i}k_{1\mathrm{x,n}} \mathrm{J}_0\left(k_{1\mathrm{rf,n}} r\right) A_{1\mathrm{U,n}}\, \mathrm{e}^{-\mathrm{i}k_{1\mathrm{x,n}}x}\, \mathrm{e}^{\mathrm{i}\omega t}, \tag{16}$$

$$u_{1\mathrm{Dx,n}} = -\mathrm{i}k_{1\mathrm{x,n}} \mathrm{J}_0\left(k_{1\mathrm{rf,n}} r\right) A_{1\mathrm{D,n}}\, \mathrm{e}^{-\mathrm{i}k_{1\mathrm{x,n}}x'}\, \mathrm{e}^{\mathrm{i}\omega t}, \tag{17}$$

$$u_{2\mathrm{x,n}} = \begin{cases} -\mathrm{i}k_{2\mathrm{x,n}} y_{1,\mathrm{n}} \mathrm{J}_0\left(k_{2\mathrm{rf,n}} r\right) A_{2,\mathrm{n}}\, \mathrm{e}^{-\mathrm{i}k_{2\mathrm{x,n}}x}\, \mathrm{e}^{\mathrm{i}\omega t},\ r < r_1 \\ -\mathrm{i}k_{2\mathrm{x,n}} \left(y_{2,\mathrm{n}} \mathrm{J}_0\left(k_{2\mathrm{rf,n}} r\right) + y_{3,\mathrm{n}} \mathrm{Y}_0\left(k_{2\mathrm{rf,n}} r\right)\right) A_{2,\mathrm{n}}\, \mathrm{e}^{-\mathrm{i}k_{2\mathrm{x,n}}x}\, \mathrm{e}^{\mathrm{i}\omega t},\ r_1 \le r < r_3 \\ -\mathrm{i}k_{2\mathrm{x,n}} \left(y_{4,\mathrm{n}} \mathrm{J}_0\left(k_{2\mathrm{rL,n}} r\right) + y_{5,\mathrm{n}} \mathrm{Y}_0\left(k_{2\mathrm{rL,n}} r\right)\right) A_{2,\mathrm{n}}\, \mathrm{e}^{-\mathrm{i}k_{2\mathrm{x,n}}x}\, \mathrm{e}^{\mathrm{i}\omega t},\ r \ge r_3 \end{cases}, \tag{18}$$

$$u_{3\mathrm{Ux,n}} = \begin{cases} -\mathrm{i}k_{3\mathrm{x,n}} \left(y_{6,\mathrm{n}} \mathrm{J}_0\left(k_{3\mathrm{rf,n}} r\right) + y_{7,\mathrm{n}} \mathrm{Y}_0\left(k_{3\mathrm{rf,n}} r\right)\right) A_{3\mathrm{U,n}}\, \mathrm{e}^{-\mathrm{i}k_{3\mathrm{x,n}}x}\, \mathrm{e}^{\mathrm{i}\omega t},\ r < r_3 \\ -\mathrm{i}k_{3\mathrm{x,n}} \left(y_{8,\mathrm{n}} \mathrm{J}_0\left(k_{3\mathrm{rL,n}} r\right) + y_{9,\mathrm{n}} \mathrm{Y}_0\left(k_{3\mathrm{rL,n}} r\right)\right) A_{3\mathrm{U,n}}\, \mathrm{e}^{-\mathrm{i}k_{3\mathrm{x,n}}x}\, \mathrm{e}^{\mathrm{i}\omega t},\ r \ge r_3 \end{cases}, \tag{19}$$

$$u_{3\mathrm{Dx,n}} = \begin{cases} -\mathrm{i}k_{3\mathrm{x,n}} \left(y_{6,\mathrm{n}} \mathrm{J}_0\left(k_{3\mathrm{rf,n}} r\right) + y_{7,\mathrm{n}} \mathrm{Y}_0\left(k_{3\mathrm{rf,n}} r\right)\right) A_{3\mathrm{D,n}}\, \mathrm{e}^{-\mathrm{i}k_{3\mathrm{x,n}}x'}\, \mathrm{e}^{\mathrm{i}\omega t},\ r < r_3 \\ -\mathrm{i}k_{3\mathrm{x,n}} \left(y_{8,\mathrm{n}} \mathrm{J}_0\left(k_{3\mathrm{rL,n}} r\right) + y_{9,\mathrm{n}} \mathrm{Y}_0\left(k_{3\mathrm{rL,n}} r\right)\right) A_{3\mathrm{D,n}}\, \mathrm{e}^{-\mathrm{i}k_{3\mathrm{x,n}}x'}\, \mathrm{e}^{\mathrm{i}\omega t},\ r \ge r_3 \end{cases}, \tag{20}$$

$$p_{1\mathrm{U,n}} = k_\mathrm{f}^2 \lambda_\mathrm{f} \mathrm{J}_0\left(k_{1\mathrm{rf,n}} r\right) A_{1\mathrm{U,n}}\, \mathrm{e}^{-\mathrm{i}k_{1\mathrm{x,n}}x}\, \mathrm{e}^{\mathrm{i}\omega t}, \tag{21}$$

$$p_{1\mathrm{D,n}} = k_\mathrm{f}^2 \lambda_\mathrm{f} \mathrm{J}_0\left(k_{1\mathrm{rf,n}} r\right) A_{1\mathrm{D,n}}\, \mathrm{e}^{-\mathrm{i}k_{1\mathrm{x,n}}x'}\, \mathrm{e}^{\mathrm{i}\omega t}, \tag{22}$$

$$p_{2,\mathrm{n}} = \begin{cases} k_\mathrm{f}^2 \lambda_\mathrm{f} y_{1,\mathrm{n}} \mathrm{J}_0\left(k_{2\mathrm{rf,n}} r\right) A_{2,\mathrm{n}}\, \mathrm{e}^{-\mathrm{i}k_{2\mathrm{x,n}}x}\, \mathrm{e}^{\mathrm{i}\omega t},\ r < r_1 \\ k_\mathrm{f}^2 \lambda_\mathrm{f} \left(y_{2,\mathrm{n}} \mathrm{J}_0\left(k_{2\mathrm{rf,n}} r\right) + y_{3,\mathrm{n}} \mathrm{Y}_0\left(k_{2\mathrm{rf,n}} r\right)\right) A_{2,\mathrm{n}}\, \mathrm{e}^{-\mathrm{i}k_{2\mathrm{x,n}}x}\, \mathrm{e}^{\mathrm{i}\omega t},\ r_1 \le r < r_3 \\ k_\mathrm{L}^2 \lambda_\mathrm{L} \left(y_{4,\mathrm{n}} \mathrm{J}_0\left(k_{2\mathrm{rL,n}} r\right) + y_{5,\mathrm{n}} \mathrm{Y}_0\left(k_{2\mathrm{rL,n}} r\right)\right) A_{2,\mathrm{n}}\, \mathrm{e}^{-\mathrm{i}k_{2\mathrm{x,n}}x}\, \mathrm{e}^{\mathrm{i}\omega t},\ r \ge r_3 \end{cases}, \tag{23}$$

$$p_{3\mathrm{U,n}} = \begin{cases} k_\mathrm{f}^2 \lambda_\mathrm{f} \left(y_{6,\mathrm{n}} \mathrm{J}_0\left(k_{3\mathrm{rf,n}} r\right) + y_{7,\mathrm{n}} \mathrm{Y}_0\left(k_{3\mathrm{rf,n}} r\right)\right) A_{3\mathrm{U,n}}\, \mathrm{e}^{-\mathrm{i}k_{3\mathrm{x,n}}x}\, \mathrm{e}^{\mathrm{i}\omega t},\ r < r_3 \\ k_\mathrm{L}^2 \lambda_\mathrm{L} \left(y_{8,\mathrm{n}} \mathrm{J}_0\left(k_{3\mathrm{rL,n}} r\right) + y_{9,\mathrm{n}} \mathrm{Y}_0\left(k_{3\mathrm{rL,n}} r\right)\right) A_{3\mathrm{U,n}}\, \mathrm{e}^{-\mathrm{i}k_{3\mathrm{x,n}}x}\, \mathrm{e}^{\mathrm{i}\omega t},\ r \ge r_3 \end{cases}, \tag{24}$$

$$p_{3\mathrm{D,n}} = \begin{cases} k_\mathrm{f}^2 \lambda_\mathrm{f} \left(y_{6,\mathrm{n}} \mathrm{J}_0\left(k_{3\mathrm{rf,n}} r\right) + y_{7,\mathrm{n}} \mathrm{Y}_0\left(k_{3\mathrm{rf,n}} r\right)\right) A_{3\mathrm{D,n}}\, \mathrm{e}^{-\mathrm{i}k_{3\mathrm{x,n}}x'}\, \mathrm{e}^{\mathrm{i}\omega t},\ r < r_3 \\ k_\mathrm{L}^2 \lambda_\mathrm{L} \left(y_{8,\mathrm{n}} \mathrm{J}_0\left(k_{3\mathrm{rL,n}} r\right) + y_{9,\mathrm{n}} \mathrm{Y}_0\left(k_{3\mathrm{rL,n}} r\right)\right) A_{3\mathrm{D,n}}\, \mathrm{e}^{-\mathrm{i}k_{3\mathrm{x,n}}x'}\, \mathrm{e}^{\mathrm{i}\omega t},\ r \ge r_3 \end{cases}. \tag{25}$$

Because the flow speed in the hydraulic line is negligible compared to the speed of sound in hydraulic fluid, the values for the reverse travelling modes in Eq. 11 to 24 can be found by replacing $A_{\mathrm{R,n}}$ with $B_{\mathrm{R,n}}$; and by replacing all instances of $k_{\mathrm{Rx,n}}$ with $-k_{\mathrm{Rx,n}}$. To differentiate, the displacement and pressures will have a superscript plus and minus added when needed to indicate modes travelling in the positive and negative axial directions.

Each mode n in a region R is characterized by a unique axial wavenumber $k_{\mathrm{Rx,n}}$. To find the wavenumber, an eigenequation must be solved in each region. For region 1, the wavenumber must satisfy a zero radial displacement condition at the outer wall; that is,

$$\left[u_{1\mathrm{r,n}}\right]_{\mathrm{r=r_0}} = 0 \quad . \tag{26}$$

Because of the negligible mean flow speed, the eigenequation has solutions of $\pm k_{\mathrm{Rx,n}}$, so it is sufficient to solve only for positive travelling modes. In region 2, five radial boundary or continuity conditions must be met, resulting in five equations that must be solved simultaneously to find the wavenumber $k_{2\mathrm{x,n}}$ as well as the relative amplitudes of $y_{1,\mathrm{n}}$ through $y_{5,\mathrm{n}}$. The conditions and corresponding equations are: zero displacement at the outer wall,

$$\left[u_{2\mathrm{r,n}}\right]_{\mathrm{r=r_2}} = 0\,, \tag{27}$$

continuity of displacement at the bladder,

$$\left[u_{2\mathrm{r,n}}\right]_{\mathrm{r=r_3-}} = \left[u_{2\mathrm{r,n}}\right]_{\mathrm{r=r_3+}}, \tag{28}$$

(r_3- and r_3+ representing the limits as r approaches r_3 from the negative and positive directions), a force balance at the bladder,

$$\begin{aligned}\left[p_2\right]_{\mathrm{r=r_3-}} &= \left[p_2 + \sigma_\mathrm{s}\ddot{u}_{2\mathrm{r}}\right]_{\mathrm{r=r_3+}} \\ &= \left[p_2 - \omega^2\sigma_\mathrm{s}u_{2\mathrm{r}}\right]_{\mathrm{r=r_3+}}\end{aligned}, \tag{29}$$

continuity of displacement at the perforate layer,

$$\left[u_{2\mathrm{r,n}}\right]_{\mathrm{r=r_1-}} = \left[u_{2\mathrm{r,n}}\right]_{\mathrm{r=r_1+}}, \tag{30}$$

and an impedance condition at the perforate layer,

$$\left[p_{2\mathrm{,n}}\right]_{\mathrm{r=r_1+}} - \left[p_{2\mathrm{,n}}\right]_{\mathrm{r=r_1-}} = Z_\mathrm{p}\left[u_{2\mathrm{r,n}}\right]_{\mathrm{r=r_1}}, \tag{31}$$

where Z_p is the measured or calculated acoustic impedance across the perforate layer. As no experimental studies were found, the perforate impedance was calculated using Eq. 21 and 29 of Bies and Hansen (2009). Omitting terms not used in the present analysis, Z_P is calculated as

$$\begin{aligned}Z_\mathrm{P} = \frac{1}{F}\Big(\pi a^2 R_\mathrm{P} + \mathrm{i}\rho_\mathrm{f}c_\mathrm{f}\,\cdot \\ \tan\left(k_\mathrm{f}w + \left(\frac{16k_\mathrm{f}a}{3\pi}\right)\left(1 - 0.43\frac{a}{q}\right)\right)\Big)\end{aligned} \tag{32}$$

where

$$R_\mathrm{P} = \frac{\rho_\mathrm{f}c_\mathrm{f}kd}{\pi a^2}\left(\frac{w}{a} + 0.288\log_{10}\left(\frac{4a^2}{h^2}\right)\right), \tag{33}$$

$$d = \sqrt{\frac{2\mu}{\rho_\mathrm{f}\omega}}, \tag{34}$$

$$\text{and } h = \max\left(\frac{w}{2}, d\right). \tag{35}$$

As the impedance formulation was derived with gaseous flow through larger orifices in mind, there is some uncertainty as to its applicability to the present case. Of particular note is the log term of R_P, which is derived from Eq. 23 of Morse and Ingard (1968). Morse and Ingard specify that the perforated plate should be much thinner than the perforate hole radius, a condition which is not met in the current case. Thus, it is uncertain whether the impedance calculation used will be sufficiently accurate.

Solving Eq. 27 to 31 simultaneously for eigenvalues $k_{2\mathrm{x,n}}$ gives the acoustic pressure and displacement for each mode in region 2. Region 3 has a similar formulation, but does not include the perforate layer:

$$\left[u_{3\mathrm{r,n}}\right]_{\mathrm{r=r_2}} = 0, \tag{36}$$

$$\left[u_{3\mathrm{r,n}}\right]_{\mathrm{r=r_3-}} = \left[u_{3\mathrm{r,n}}\right]_{\mathrm{r=r_3+}}, \tag{37}$$

$$\text{or } \left[p_3\right]_{\mathrm{r=r_3-}} = \left[p_3 - \omega^2\sigma_\mathrm{s}u_{3\mathrm{r}}\right]_{\mathrm{r=r_3+}}. \tag{38}$$

Given a finite number of radial modes N, the modal amplitudes $A_{\mathrm{R,n}}$ and $B_{\mathrm{R,n}}$ can be found by simultaneously solving a number of equations which provide for pressure and axial displacement continuity at the region boundaries. The number of equations is reduced by letting all $B_{1\mathrm{D,n}}= 0$ due to an assumption of an anechoic termination. Additionally, it is assumed that incoming evanescent waves $A_{1\mathrm{U,n}}$ have zero amplitude at $x = 0$, with the exception of excitation plane wave $A_{1\mathrm{U,0}}$, which is the reference input and is arbitrarily set to unity. To further simplify, the rigid region 3 wall boundaries at $x = -L_1$ and $x = L + L_2$ allow for the immediate substitutions

$$A_{3\mathrm{U,n}} = B_{3\mathrm{U,n}}\mathrm{e}^{-2\mathrm{i}k_{3\mathrm{x,n}}\mathrm{L_1}}, \tag{39}$$

$$B_{3\mathrm{D,n}} = A_{3\mathrm{D,n}}\mathrm{e}^{-2\mathrm{i}k_{3\mathrm{x,n}}\mathrm{L_2}}. \tag{40}$$

The other axial equations are in the form of area integrals:

$$\begin{aligned}&\int_0^{\mathrm{r_{a,m}}}\sum_{\mathrm{n=0}}^{\mathrm{N-1}}\left(\left[p_{1\mathrm{U,n}}^{+}\right]_{\mathrm{x=0}} + \left[p_{1\mathrm{U,n}}^{-}\right]_{\mathrm{x=0}}\right)rdr \\ &= \int_0^{\mathrm{r_{a,m}}}\sum_{\mathrm{n=0}}^{\mathrm{N-1}}\left(\left[p_{2\mathrm{,n}}^{+}\right]_{\mathrm{x=0}} + \left[p_{2\mathrm{,n}}^{-}\right]_{\mathrm{x=0}}\right)rdr,\end{aligned} \tag{41}$$

$$\begin{aligned}&\int_0^{\mathrm{r_{a,m}}}\sum_{\mathrm{n=0}}^{\mathrm{N-1}}\left(\left[p_{1\mathrm{D,n}}^{+}\right]_{\mathrm{x=L}} + \left[p_{1\mathrm{D,n}}^{-}\right]_{\mathrm{x=L}}\right)rdr \\ &= \int_0^{\mathrm{r_{a,m}}}\sum_{\mathrm{n=0}}^{\mathrm{N-1}}\left(\left[p_{2\mathrm{,n}}^{+}\right]_{\mathrm{x=L}} + \left[p_{2\mathrm{,n}}^{-}\right]_{\mathrm{x=L}}\right)rdr,\end{aligned} \tag{42}$$

$$\begin{aligned}&\int_{r_1}^{\mathrm{r_{c,m}}}\sum_{\mathrm{n=0}}^{\mathrm{N-1}}\left(\left[p_{3\mathrm{U,n}}^{+}\right]_{\mathrm{x=0}} + \left[p_{3\mathrm{U,n}}^{-}\right]_{\mathrm{x=0}}\right)rdr \\ &= \int_{r_1}^{\mathrm{r_{c,m}}}\sum_{\mathrm{n=0}}^{\mathrm{N-1}}\left(\left[p_{2\mathrm{,n}}^{+}\right]_{\mathrm{x=0}} + \left[p_{2\mathrm{,n}}^{-}\right]_{\mathrm{x=0}}\right)rdr,\end{aligned} \tag{43}$$

$$\begin{aligned}&\int_{r_1}^{\mathrm{r_{c,m}}}\sum_{\mathrm{n=0}}^{\mathrm{N-1}}\left(\left[p_{3\mathrm{D,n}}^{+}\right]_{\mathrm{x=L}} + \left[p_{3\mathrm{D,n}}^{-}\right]_{\mathrm{x=L}}\right)rdr \\ &= \int_{r_1}^{\mathrm{r_{c,m}}}\sum_{\mathrm{n=0}}^{\mathrm{N-1}}\left(\left[p_{2\mathrm{,n}}^{+}\right]_{\mathrm{x=L}} + \left[p_{2\mathrm{,n}}^{-}\right]_{\mathrm{x=L}}\right)rdr,\end{aligned} \tag{44}$$

$$\int_{0}^{r_{b,m}} \sum_{n=0}^{N-1} \left(\left[u_{2x,n}^{+} \right]_{x=0} + \left[u_{2x,n}^{-} \right]_{x=0} \right) r dr = \begin{cases} \int_{0}^{r_{b,m}} \sum_{n=0}^{N-1} \left(\left[u_{1Ux,n}^{+} \right]_{x=0} + \left[u_{1Ux,n}^{-} \right]_{x=0} \right) r dr, \; r_b < r_0 \\ U_U, \; r_0 \le r_b < r_1 \\ U_U + \int_{r_1}^{r_{b,m}} \sum_{n=0}^{N-1} \left(\left[u_{3Ux,n}^{+} \right]_{x=0} + \left[u_{3Ux,n}^{-} \right]_{x=0} \right) r dr, \; r_b \ge r_1 \; , \end{cases} \tag{45}$$

$$\int_{0}^{r_{b,m}} \sum_{n=0}^{N-1} \left(\left[u_{2x,n}^{+} \right]_{x=L} + \left[u_{2x,n}^{-} \right]_{x=L} \right) r dr = \begin{cases} \int_{0}^{r_{b,m}} \sum_{n=0}^{N-1} \left(\left[u_{1Dx,n}^{+} \right]_{x=0} + \left[u_{1Dx,n}^{-} \right]_{x=0} \right) r dr, \; r_b < r_0 \\ U_D, \; r_0 \le r_b < r_1 \\ U_D + \int_{r_1}^{r_{b,m}} \sum_{n=0}^{N-1} \left(\left[u_{3Dx,n}^{+} \right]_{x=L} + \left[u_{3Dx,n}^{-} \right]_{x=L} \right) r dr, \; r_b \ge r_1 \; , \end{cases} \tag{46}$$

$$U_U = \int_{0}^{r_0} \sum_{n=0}^{N-1} \left(\left[u_{1Ux,n}^{+} \right]_{x=0} + \left[u_{1Ux,n}^{-} \right]_{x=0} \right) r dr \; , \tag{47}$$

$$U_D = \int_{0}^{r_0} \sum_{n=0}^{N-1} \left(\left[u_{1Dx,n}^{+} \right]_{x=L} + \left[u_{1Dx,n}^{-} \right]_{x=L} \right) r dr \; , \tag{48}$$

$$\begin{aligned} r_{a,m} &= \frac{m+1}{M} r_0, \quad r_{b,m} \\ &= \frac{m+1}{M} r_2, \quad r_{c,m} \\ &= r_1 + \frac{m+1}{M} \left(r_2 - r_1 \right) \end{aligned} \tag{49}$$

where m = 0 to M-1, and M = N. It may be noted here that in addition to the direct integration method shown in Eq. 41 through 49, weighted integral methods are also commonly found in the literature. As successful examples of both methods of mode matching can be easily found (Denia et al., 2007; Nennig et al., 2010; Selamet et al., 2004; Selamet et al., 2005; Xu et al., 2003), it is simply noted that the chosen method was convenient for the present analysis.

The solution of Eq. 41 to 49 gives all the unknown complex modal amplitudes. Using the known excitation amplitude and the calculated transmitted wave amplitude $A_{1D,0}$, acoustic transmission loss (TL) can be found as

$$TL = -10 \log_{10} \left(\left| T_A \right|^2 \right), \tag{50}$$

where

$$T_A = \frac{A_{1D,0}}{A_{1U,0}} \; . \tag{51}$$

4 Experiment

To validate the analytical model predictions, a commercially available suppressor, Wilkes & McLean model WM-5081 was purchased and tested. A model WM-3081 was purchased and deconstructed to determine internal dimensions; it is rated for a lower pressure than the WM-5081 and therefore has a different casing, but the two models have the same internal structure as far as could be determined. The WM-5081 device was non-destructively disassembled, and all measurable dimensions were consistent with the WM-3081 device. Specifically, the bladder mass and internal shell radius could not be measured without potentially damaging the device, but there is no obvious cause to believe that they differ between devices. The relevant dimensions and measurements for the suppressor are found in Table 1, including bladder measurements for finding σ_s. Additional dimensions were measured for the thin perforated sheet, shown in Table 2, in order to estimate Z_p. The hydraulic fluid used in these tests has density ρ_f = 866 kg m^{-3} and sound speed c_f = 1400 m s^{-1}. The kinematic viscosity of the fluid is published to be 46.0 cSt at 40°C and 6.8 cSt at 100°C and a linear fit is taken for experimentally measured temperatures. The frequencies of interest for model validation are from 0 to 2000 Hz but data are collected up to 5400 Hz for further validation and to observe possible trends at higher frequencies. The test setup and methodology are detailed in the following:

Table 1: Suppressor dimensions

Inlet Pipe Radius r_0 (m)	0.0103
Uncompressed Inner Radius r_1 (m)	0.0173
Outer Radius r_2 (m)	0.0262
Length L (m)	0.0450
Inlet extension L_1 (m)	0.0185
Outlet extension L_2 (m)	0.0185
Bladder total mass (kg)	0.038
Bladder total length (m)	0.112

Table 2: Perforate layer dimensions and features

Perforate layer thickness w (m)	0.0006
Perforate hole radius a (m)	0.0005
Perforate hole separation q (m)	0.0020
Perforate hole area fraction F	0.227

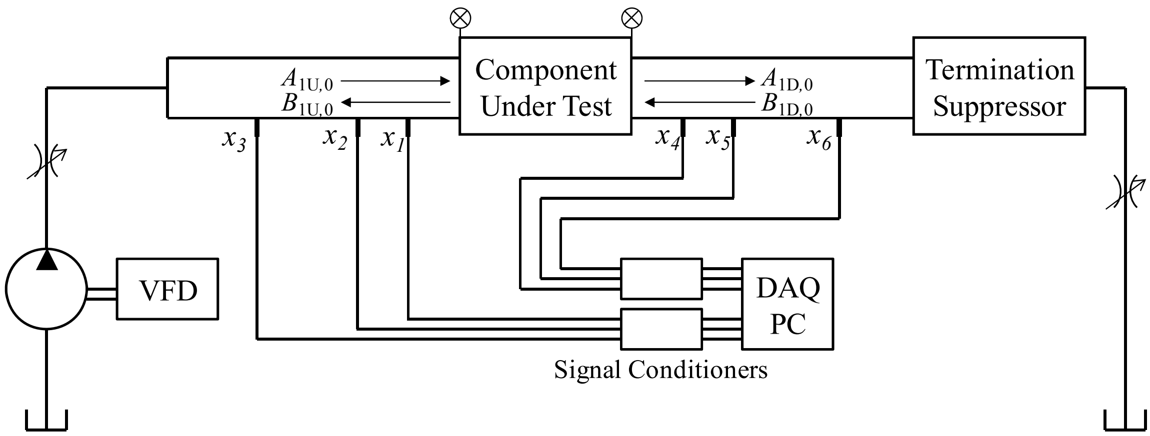

Fig. 5: *Schematic of test setup for measurement of fluid acoustic properties of a suppressor under test*

4.1 Test Setup

The test rig at the Georgia Institute of Technology is built in accordance with the ISO-15086-2 (2000) standard. A schematic of the test rig can be seen in Fig. 5. Flow is provided to the system at 40 liters per minute from a 9 piston axial piston pump driven by a variable frequency drive (VFD). Upstream of the test section, a partially closed needle valve provides broadband noise to the test section. The test section includes two rigid pipe sections of 0.0191 m (0.75 in) inner diameter with the test device between them. The system has six piezoelectric pressure sensors, labeled in Fig. 5 as x_1 to x_6. Each piezoelectric sensor is mounted flush with the inside of the test section. The data from each sensor are collected by a data acquisition card (DAQ) mounted inside of a PC. Data are captured at 10800 samples/second and each sample record is 5120 samples long. Every test run is a vector average of 100 sample records. Two static pressure sensors are mounted in the system, one immediately upstream of the test suppressor and the other immediately downstream of the test suppressor. The difference between the sensors is the pressure loss across the device, which is found to be within the sensor resolution of 70 kPa (10 psi). A termination suppressor is connected downstream of the test section, and isolates the test section from downstream noise, ensuring high coherence in the transfer functions between the piezoelectric sensors. A second needle valve is located downstream of the termination suppressor. This needle valve is used to load the system to a given static pressure. A thermocouple measures the temperature of the hydraulic fluid for each test; the temperature of the compressed gas in the test suppressor is estimated to be approximately the temperature of the hydraulic fluid when the gas is added.

4.2 Test Method

The upstream and downstream wave fields must be known to calculate the transmission loss across the test suppressor. Figure 5 shows the wave fields in the test section but for testing purposes, only the plane wave modes in the upstream and downstream pipes are needed To avoid the half-wavelength indeterminacy that is present with two sensors, the multi-point method with three sensors is used (Johnston et al., 1994). Transfer functions are used to compare the pressure between each sensors, eliminating the need for absolute calibration.

A least-squares regression of the sensor data approximates the wave amplitudes of both the upstream and downstream test sections. This method is further discussed by Earnhart and Cunefare (2012). Acoustic pressure p_1 and volume velocity Q_1 at the upstream port are related to p_2 and Q_2 at the downstream ports by a transfer matrix with elements t_{ij}:

$$\begin{pmatrix} p_1 \\ Q_1 \end{pmatrix} = \begin{bmatrix} t_{11} & t_{12} \\ t_{21} & t_{22} \end{bmatrix} \begin{pmatrix} p_2 \\ Q_2 \end{pmatrix}. \tag{52}$$

Pressure and velocity can be calculated from the wave amplitudes using the equations

$$\begin{aligned} p_1 &= A_{1U,0} + B_{1U,0} \qquad p_2 = A_{1D,0} + B_{1D,0} \\ Q_1 &= \frac{A_{1U,0} - B_{1U,0}}{Z_0} \qquad Q_2 = \frac{A_{1D,0} - B_{1D,0}}{Z_0}, \end{aligned} \tag{53}$$

where $A_{R,0}$ and $B_{R,0}$ are the forward-and reverse-traveling wave amplitudes as defined in the theoretical model, and where

$$Z_0 = \frac{\rho_f c_f}{\pi r_0^2} \tag{54}$$

is the acoustic impedance, ρ_f is the density of the fluid, c_f is the speed of sound in the fluid, and r_0 is the inner radius of the pipe.

Using Eq. 52 to 54, the elements of the transfer matrix can be calculated and placed into the transmission loss equation:

$$TL = 20\log_{10} \frac{1}{2}\left| t_{11} + \frac{t_{12}}{Z_0} + Z_0 t_{21} + t_{22} \right| \tag{55}$$

Equation 55 can be simplified by assuming that the test suppressor is geometrically symmetric end to end, and that the system is assumed to be reciprocal, resulting in

$$t_{11} = t_{22},\ t_{21} = \frac{1+t_{11}^2}{t_{12}}. \tag{56}$$

Applying Eq. 56 to Eq. 52 to 55 yields the new *TL* equation

$$TL = 20\log_{10}\left|\frac{A_{1U,0}^2 - B_{1D,0}^2}{A_{1U,0}A_{1D,0} - B_{1U,0}B_{1D,0}}\right|. \tag{57}$$

5 Results

5.1 Modeling Results

As several new features have been added to existing methods to create the present model, it is of interest to determine their effect on transmission loss performance. First, the mass of the rubber bladder is considered. The total mass contained in the expansion area is uncertain; the expansion length L_T is 0.73 times the total bladder length, but the effective mass of the bladder will be less than this fraction because the bladder thickens into rings at each end, resulting in a nonuniform mass distribution per length. It is estimated that using 0.5 times the measured bladder mass, 0.019 kg, in Eq. 5 will approximately account for the bladder sheet density. To test the sensitivity of this estimate to errors, simulations have been run for m_b equal to 0.019, 0.027, and 0.038 kg, as shown in Fig. 6. Although differences of around 4 dB are observed above 3000 Hz, the differences are kept below about 1.5 dB below 2000 Hz. The results are therefore relatively insensitive to changes in bladder mass, especially at low frequencies; and any error in the bladder estimation should not cause significant error in the transmission loss predictions.

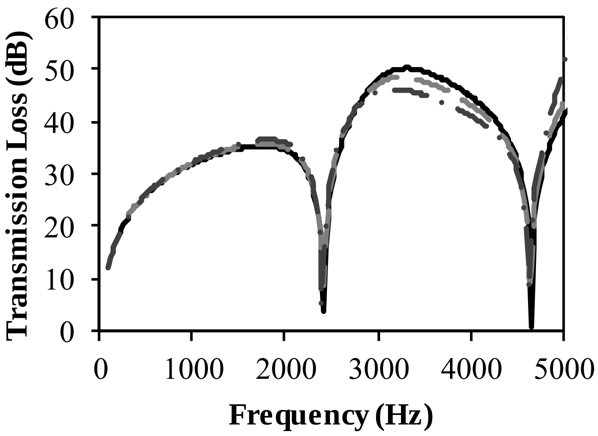

Fig. 6: *Study of bladder mass, P_s = 10.3 MPa, P_c = 5.2 MPa, no perforate layer.* ▬ *m_b = 0.019 kg;* ▬ ▬ *m_b = 0.027 kg;* ▬ ▪ *m_b = 0.038 kg*

In addition, temperature affects the compressibility of the nitrogen and may have important effects on transmission loss. Although the system temperature during testing is measured, there is some uncertainty in the temperature when the bladder is initially pressurized up to P_c, which affects the calculated mass of the nitrogen and bladder radius r_3. For a system running at 36°C, precharge temperatures of 20°C and 40°C are simulated in Fig. 7 to determine the sensitivity to precharge temperature. As can be observed, the differences are minimal over the whole range of 0 to 5000 Hz, and it is thus concluded that uncertainty or reasonable variation in bladder precharge temperature will not significantly affect transmission loss predictions.

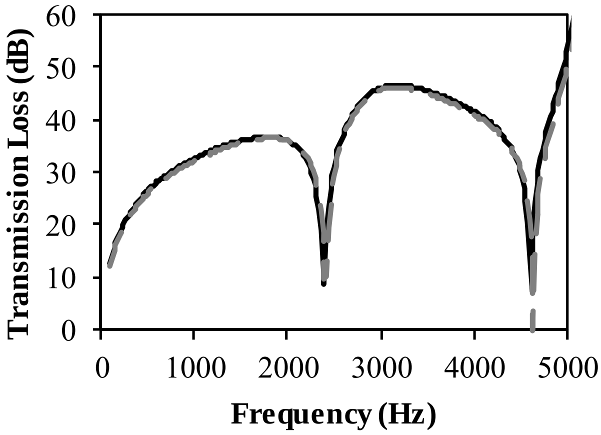

Fig. 7: *Temperature study, P_s = 10.3 MPa, P_c = 5.2 MPa, no perforate layer, system temperature = 36°C. Nitrogen precharge temperature:* ▬ *20°C;* ▬ ▬ *40°C*

Finally, sensitivity to the perforate layer is investigated. While the validity of the current perforate impedance model is called into question, the model may nevertheless give some indication of the importance and probable effects of the perforate layer. Two simulations are shown in Fig. 8, where the only difference is inclusion of the perforate layer. The difference between the models is clear, reaching 5 dB at a frequency of about 1500 Hz, and continuing to show significant deviation at higher frequencies. To help determine the validity of the current perforate model, results are shown with and without the perforate layer in the experimental validation section.

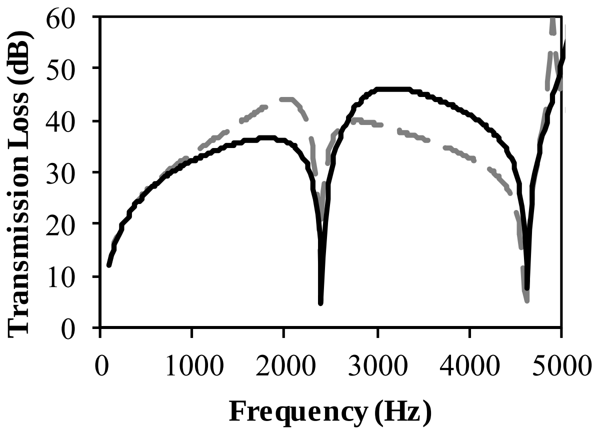

Fig. 8: *Perforate layer impedance study, P_s = 10.3 MPa, P_c = 5.2 MPa.* ▬ *No perforate layer;* ▬ ▬ *Includes perforate layer impedance*

5.2 Experimental Validation

To validate the model experimentally, tests were run on the experimental rig at various system and bladder precharge pressures. Fig. 9 shows the validation for a system pressure of P_s = 10.3 MPa and a precharge pressure of P_c = 2.1 MPa. In Figs. 10 and 11, P_s is maintained, but P_c is increased to 3.1 MPa, and to the manufacturer recommended 0.5 P_s, or 5.2 MPa, respectively. In Fig. 12, the P_c ratio is maintained at 0.5 P_s, with P_s being increased to 20.7 MPa, and P_c at 10.3 MPa. Dips in measured transmission loss in all three cases are seen around 500 and 900 Hz; these are artifacts of the test setup and should not be observed in the model predictions.

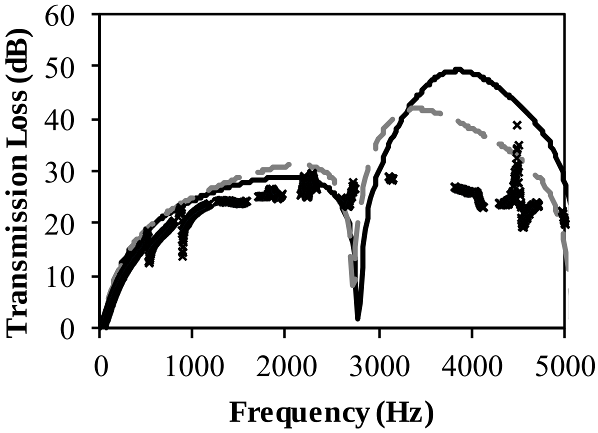

Fig. 9: *P_s = 10.3 MPa, P_c = 2.1 MPa. x Experimental data; ▬ Simulation, no perforate layer; ▬ ▬ Simulation, includes perforate layer impedance*

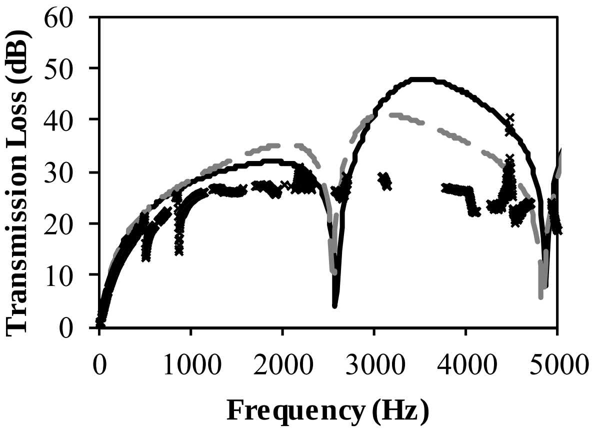

Fig. 10: *P_s = 10.3 MPa, P_c = 3.1 MPa. x Experimental data; ▬ Simulation, no perforate layer; ▬ ▬ Simulation, includes perforate layer impedance*

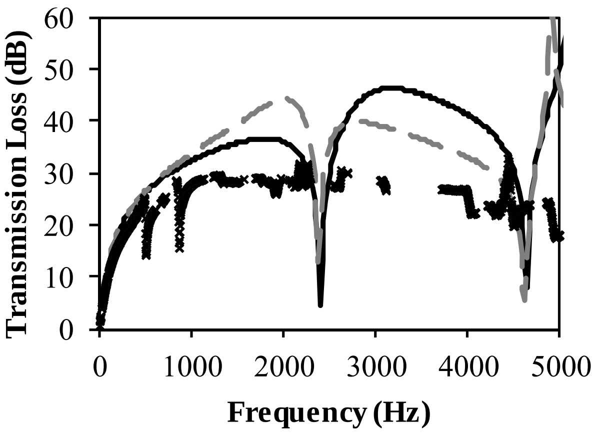

Fig. 11: *P_s = 10.3 MPa, P_c = 5.2 MPa. x Experimental data; ▬ Simulation, no perforate layer; ▬ ▬ Simulation, includes perforate layer impedance*

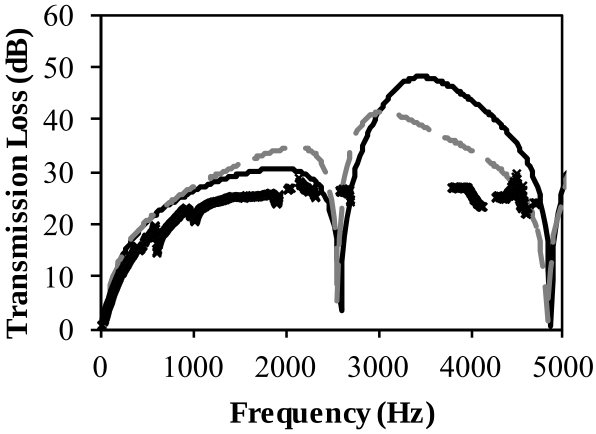

Fig. 12: *P_s = 20.7 MPa, P_c = 10.3 MPa. x Experimental data; ▬ Simulation, no perforate layer; ▬ ▬ Simulation, includes perforate layer impedance*

In Fig. 9 to 12, the simulation with the perforate layer shows less agreement with low frequency experimental data than the simulation that omits the perforate layer. Also, at low frequencies (below 2000 Hz) better agreement is observed with experimental data when the precharge pressure is lower (Fig. 9 to 11); or, considering the same relative precharge percentage, when the total pressure is higher (Fig. 11 and 12); though with the small number of data sets this trend should perhaps be treated with some caution. Notably, experimental agreement becomes very poor at the predicted transmission loss dip around 2500 Hz, and generally above 2000 Hz, especially as the predicted transmission loss increases. The lack of an experimental transmission loss dip around 2500 Hz could be indicative of insufficiently modeled system damping; the large divergence between model and experiment at higher frequencies may indicate flanking transmission paths or unmodeled phenomena that become significant at higher frequencies. This may indicate a need for improved perforate layer models, or for more complex models of the rubber bladder behavior. Nevertheless, the model is accurate within 5 dB up to about 1300 Hz for all tests with system pressures of at least 10.3 MPa and bladder precharge pressures up to 0.5 times system pressure, and up to about 2300 Hz for three of the cases. This makes it useful for at least the first several harmonics of many axial piston pumps, which are commonly used in the hydraulics industry.

6 Conclusions

The presented theoretical model has been shown to correspond well to experimental data at frequencies below about 1300 to 2300 Hz, depending on system and precharge pressure conditions. This frequency range is relevant to noise sources in many hydraulic power applications. In addition, simulations show that the impedance of the perforate layer affects transmission loss much more than small variations in bladder precharge temperature or variations in rubber bladder mass. However, since better experimental agreement is obtained when the model omits the perforate layer, it is concluded that better perforate layer impedance models or experimental data are still needed. Additionally, changes to include the stiffness of the rubber bladder might improve high frequency experimental correlations.

Nomenclature

$A_{R,n}$	Forward travelling modal amplitude coefficient for mode n in region R	
$B_{R,n}$	Reverse travelling modal amplitude coefficient for mode n in region R	
F	Perforate hole area fraction	
J_i	Bessel function of the first kind, of order i	
L	Length of main suppressor cavity	[m]
L_1, L_2	Length of inlet, outlet extensions	[m]
L_T	Length of main suppressor cavity plus inlet and outlet extensions	[m]
M	Maximum value of m	
M_N	Molar mass of nitrogen	[kg mol^{-1}]
N	Maximum number of modes considered in simulation	
P_c	Bladder precharge pressure	[Pa]
Ps	Hydraulic system pressure	[Pa]
Q_1, Q_2	Average acoustic volume velocities at upstream, downstream ports	[m3 s^{-1}]
R	Region number, as defined in Fig. 3	
R	Universal gas constant	
T	Working system temperature	[C]
T_0	Precharge nitrogen temperature	[C]
T_A	Acoustic transmission coefficient	
T_L	Acoustic transmission loss	[dB]
$U_{U,\,UD}$	Integrals used in some mode matching equations	
V_0	Original nitrogen volume	[m3]
Y_i	Bessel function of the second kind, of order i	
Z_0	Acoustic impedance in pipe	[kg m^{-4} s^{-1}]
Z_p	Perforate layer impedance	[kg m^{-4} s^{-1}]
a	Perforate hole radius	[m]
c_f, c_L	Sound speed in hydraulic fluid, nitrogen	[m s^{-1}]
d	Boundary layer thickness	[m]
h	Length parameter	[h]
k_f, k_L	Wavenumber in hydraulic fluid, nitrogen	[m^{-1}]
$k_{Rrf,n}$, $k_{RrL,n}$	Radial decomposition of wavenumber in hydraulic fluid or nitrogen, for mode n in region R	[m^{-1}]
$k_{Rx,n}$	Axial decomposition of wavenumber for mode n in region R	[m^{-1}]
m_b	Bladder mass	[kg]
m	Total nitrogen mass	[kg]
m	Integration iterator for mode matching	
n	Mode number subscript	
p_1, p_2	Average acoustic pressures at upstream, downstream ports	[Pa]
$p_{R,n}$	Acoustic pressure of mode n in region R	[Pa]
q	Perforate hole separation distance	[m]
r_0	Inlet and outlet pipe radius	[m]
r_1	Perforate layer radius	[m]
r_2	Inner radius of outer shell	[m]
r_3	Radius of bladder when system is pressurized	[m]
r_a, r_b, r_c	Iterated radii in mode matching integrals	[m]
t_{ij}	Transfer matrix coefficients	
$u_{Rx,n}$, $u_{Rr,n}$	Axial, radial acoustic displacement of mode n in region R	[m s^{-1}]
w	Perforate layer thickness	[m]
x	Axial coordinate	[m]
x'	Adjusted axial coordinate	[m]
x_1 - x_6	Pressure transducer labels	
$y_{1,n}$ - $y_{9,n}$	Relative amplitude coefficients of displacement and pressure terms	
λ_f, μ_f	Lamé parameters of hydraulic fluid	[Pa]
λ_L, μ_L	Lamé parameters of nitrogen	[Pa]
μ	Fluid dynamic viscosity	[Pa s]
ρ_f, ρ_L	Density of hydraulic fluid, nitrogen	[kg m^{-3}]
σ_s	Sheet density of bladder	[kg m^{-2}]
ω	Angular frequency of acoustic signal	[s^{-1}]

Acknowledgements

This research was supported by the Center for Compact and Efficient Fluid Power, a National Science Foundation Engineering Research Center funded under cooperative agreement number EEC-0540834.

References

Arendt, E. 1988. *Pulsation absorbing device*, USA Patent No. 4,759,387.

Bies, D. A. and **Hansen, C. H.** 2009. *Engineering Noise Control: Theory and Practice*, Spon Press, New York, 2009.

Bilawchuk, S. and **Fyfe, K. R.** 2003. Comparison and implementation of the various numerical methods used for calculating transmission loss in silencer systems. *Applied Acoustics*, Vol. 64, pp. 903-916.

Cummings, A. and **Chang, I.-J.** 1988. Sound attenuation of a finite length dissipative flow duct silencer with internal mean flow in the absorbent. *Journal of Sound and Vibration*, Vol. 127, pp. 1 - 17.

Denia, F. D., **Selamet, A.**, **Fuenmayor, F. J.** and **Kirby, R.** 2007. Acoustic attenuation performance of perforated dissipative mufflers with empty inlet/outlet extensions. *Journal of Sound and Vibration*, Vol. 302, pp. 1000 - 1017.

Dexter, E. 1985. *Pulsation dampener and acoustic attenuator*, USA Patent No. 4,497,388.

Dickey, N. S., **Selamet, A.** and **Ciray, M. S.** 2001. An experimental study of the impedance of perforated plates with grazing flow. *Journal of the Acoustical Society of America*, Vol. 110, pp. 2360 - 2370.

Earnhart, N. E. and **Cunefare, K. A.** 2012. Compact Helmholtz resonators for hydraulic systems. *International Journal of Fluid Power*, Vol. 13, pp. 41 - 50.

Jenski, J., **Gary M.** and **Shiery, J. C.** 1998. *Noise suppressor*, USA Patent No. 5,735,313.

Johnston, D. N., **Longmore, D. K.** and **Drew, J. E.** 1994. A technique for the measurement of the transfer matrix characteristics of two-port hydraulic components. *Fluid Power Systems and Technology*, Vol. 1, pp. 25 - 33.

Kirby, R. 2001. Simplified techniques for predicting the transmission loss of a circular dissipative silencer. *Journal of Sound and Vibration*, Vol. 243, pp. 403 - 426.

Kirby, R. and **Cummings, A.** 1998. The impedance of perforated plates subjected to grazing gas flow and backed by porous media. *Journal of Sound and Vibration*, Vol. 217, pp. 619 - 636.

Kirby, R. and **Denia, F. D.** 2007. Analytic mode matching for a circular dissipative silencer containing mean flow and a perforated pipe. *Journal of the Acoustical Society of America*, Vol. 122, pp. 3471 - 3482.

Lee, I., **Selamet, A.** and **Huff, N. T.** 2006. Acoustic impedance of perforations in contact with fibrous material. *Journal of the Acoustical Society of America*, Vol. 119, pp. 2785 - 2797.

Lee, I., **Selamet, A.** and **Huff, N. T.** 2006. Impact of perforation impedance on the transmission loss of reactive and dissipative silencers. *Journal of the Acoustical Society of America*, Vol. 120, pp. 3706 - 3713.

Morse, P. M. and **Ingard, K. U.** 1968. *Theoretical Acoustics*, McGraw-Hill, Inc., New York, 1968.

Nennig, B., **Perrey-Debain, E.** and **Ben Tahar, M.** 2010. A mode matching method for modeling dissipative silencers lined with poroelastic materials and containing mean flow. *Journal of the Acoustical Society of America*, Vol. 128, pp. 3308 - 3320.

Panigrahi, S. N. and **Munjal, M. L.** 2005. Comparison of various methods for analyzing lined circular ducts. *Journal of Sound and Vibration*, Vol. 285, pp. 905 - 923.

Peat, K. S. 1991. A transfer matrix for an absorption silencer element. *Journal of Sound and Vibration*, Vol. 146, pp. 353 - 360.

Rabie, M. G. 2007. On the application of oleopneumatic accumulators for the protection of hydraulic transmission lines against water hammer - a theoretical study. *International Journal of Fluid Power*, Vol. 8, pp. 39 - 49.

Selamet, A. and **Ji, Z. L.** 1999. Acoustic attenuation performance of circular expansion chambers with extended inlet/outlet. *Journal of Sound and Vibration*, Vol. 223, pp. 197 - 212.

Selamet, A., **Xu, M. B.**, **Lee, I. - J.** and **Huff, N. T.** 2004. Analytical approach for sound attenuation in perforated dissipative silencers. *Journal of the Acoustical Society of America*, Vol. 115, pp. 2091 - 2099.

Selamet, A., **Xu, M. B.**, **Lee, I. - J.** and **Huff, N. T.** 2005. Analytical approach for sound attenuation in perforated dissipative silencers with inlet/outlet extensions. *Journal of the Acoustical Society of America*, Vol. 117, pp. 2078 - 2089.

Shiery, J. C. 1998. *Noise suppressor*, USA Patent No. 5,732,741.

International Organization for Standardization, 2000. ISO 15086-2, *Hydraulic fluid power - Determination of fluid-borne noise characteristics of components and systems - Part 2: Measurement of speed of sound in a fluid in a pipe*.

Sullivan, J. W. and **Crocker, M. J.** 1978. Analysis of concentric-tube resonators having unpartitioned cavities. *Journal of the Acoustical Society of America*, Vol. 64, pp. 207 - 215.

Wilkes, R. Year. Noise Reduction in Hydraulic Systems, *Inter-Noise 95*, Vol. Newport Beach, CA, USA, pp. 93 - 96.

Xu, M. B., **Selamet, A.**, **Lee, I. - J.** and **Huff, N. T.** 2003. Sound attenuation in dissipative expansion chambers. *Journal of Sound and Vibration*, Vol. 272, pp. 1125 - 1133.

Yokota, S., **Somada, H.** and **Yamaguchi, H.** 1996. Study on an active accumulator. *JSME International Journal*, Vol. Series B, Vol 39, pp. 119 - 124.

Kenneth Marek
has a BSME degree from Texas Tech University and is currently a Ph.D. candidate in Mechanical Engineering at the Georgia Institute of Technology. His research focuses on modeling and simulation of noise control technologies for fluid power.

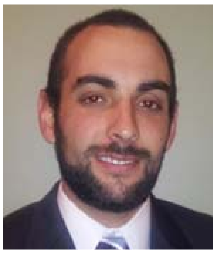

Elliott Gruber
earned a BSME degree from the Georgia Institute of Technology in 2007. He is currently pursuing a Ph. D. in Mechanical Engineering, also at the Georgia Institute of Technology.

Dr. Cunefare
is a Professor at the Georgia Institute of Technology. He began at Georgia Tech in 1990. Prior he was the F.V. Hunt Postdoctoral Fellow at The Technical University of Berlin. He earned his PhD in 1990 from the Pennsylvania State University. He is currently Professor in Charge of the Integrated Acoustics Laboratory.